Aberrated electron probes for magnetic spectroscopy with atomic resolution: Theory and practical aspects

Ján Rusz[1] and Juan Carlos Idrobo[2]

[1]*Department of Physics and Astronomy, Uppsala University, P.O. Box 516, 75120 Uppsala, Sweden*

[2]*Center of Nanophase Materials Sciences, Oak Ridge National Laboratory, Oak Ridge, Tennessee 37831, USA*

(Received 20 December 2015; revised manuscript received 26 February 2016; published 24 March 2016)

It was recently proposed that electron magnetic circular dichroism can be measured in scanning transmission electron microscopy with atomic resolution by tuning the phase distribution of an electron beam. Here, we describe the theoretical and practical aspects for the detection of out-of-plane and in-plane magnetization utilizing atomic size electron probes. We present the calculated optimized astigmatic probes and discuss how to achieve them experimentally.

DOI: 10.1103/PhysRevB.93.104420

I. INTRODUCTION

Electron magnetic circular dichroism (EMCD) is a relatively young experimental technique, proposed in 2003 [1] along the lines of symmetry-selected electron energy-loss spectroscopy (EELS) [2]. The first experimental measurements were performed in 2006 in transmission electron microscopy (TEM), using a plane wave illumination [3], with spatial resolution of ∼100 nm. The use of TEM to measure an EMCD signal implied that, in principle, higher spatial resolutions—subnanometer or even atomic-resolution level—could be achieved under the right electron optical configurations. However, the intrinsic low EMCD signal strength has caused a slow adoption of the technique, despite the initial experimental successes [4–12] and theoretical development [13–17].

The field of EMCD experienced a new wave of attention in 2010, when electron vortex beams (EVBs) were achieved in electron microscopy [18–20] following the 2007 prediction by Bliokh *et al.*[21]. Intense research followed since, however, no EMCD measurements have been achieved with EVBs, except for the initial report by Verbeeck *et al.*[20], and a second work from the same laboratory [22]. Later, in 2013, on the basis of theoretical calculations, it was proposed that using EVBs for measuring EMCD on crystals is not efficient, unless the EVBs are of atomic size [23]. The study was soon followed by a similar work [24], which instead of a crystal lattice focused on isolated atoms or small nanoparticles. A detailed survey of expected EMCD strength measured by EVBs [25] was also published, proposing optimized measurement conditions for bcc iron. All the theoretical studies suggest that in order to detect an EMCD signal in EELS in the transmitted (direct) beam direction, EVBs must have an atomic size and pass directly through—or very close to (within less than approximately half of an Å)—an atomic column carrying an effective magnetic moment. As of today (early 2016), isolated atomic-size EVBs that can be used for EMCD measurements have not been achieved experimentally, although several ways of generating them have been suggested [26–31].

Very recently, the appearance of an EMCD signal in EELS at the transmitted beam direction was predicted under specific diffraction interference and phase distribution of the electron probe [32]. The theoretical prediction indicated that the suitable conditions for observing an EMCD signal in a conventional EELS-STEM experiment can be summarized by the following two points: (1) The convergent electron-beam diffraction (CBED) pattern must show overlapping disks. In other words, the convergence angle α must be larger than $G\lambda/2$, where G is the length of a reciprocal-lattice vector corresponding to the shortest allowed reflection, and λ is the de Broglie wavelength of electrons. This is also the necessary condition for achieving atomic resolution in scanning transmission electron microscopy (STEM) [33]. (2) If $\chi_{\mathbf{k}'}$ is the phase of an individual $\mathbf{k}'$-vector component of the convergent electron beam, and also the mirror image of $\mathbf{k}$ with respect to a selected mirror symmetry plane, then the phase differences $\Delta\chi_{\mathbf{k},\mathbf{G}} = \chi_{\mathbf{k}+\mathbf{G}} - \chi_{\mathbf{k}}$ should change sign under the mirror symmetry operation: $\Delta\chi_{\mathbf{k},\mathbf{G}} = -\Delta\chi_{\mathbf{k}',\mathbf{G}}$. This second condition should be fulfilled for all $\mathbf{k}$ and all mirror planes [34]. EVBs fulfill the second condition regardless of the symmetry of the sample. In this sense, a vortex is a universal beam shape that can be used to measure EMCD on any magnetic crystals magnetized along the beam direction, assuming that the electron probe is sufficiently small.

The same theoretical work [32] also proposed an alternative approach to detecting an EMCD signal in EELS, completely avoiding the necessity to generate atomic-size vortex beams. The alternative approach simply requires a suitable phase distribution of the electron probe, which can be achieved by aberration-correcting STEM. There is no necessity of any modification of the STEM column. For example, it was shown that for a cubic or a tetragonal crystal aligned in the (001) orientation, a nonzero fourfold astigmatism (labeled here as $C_{3,4b}$ following Krivanek's notation [35]) will lead to a detectable EMCD signal in atomically resolved spectrum images in STEM experiments. Not only it is easier to set up such aberrated probes in modern STEMs, since no hardware modifications are needed, but in addition, the whole beam intensity can be used when acquiring the EEL spectra—contrary to fork [19,20,36,37] or spiral apertures [28,29], or phase masks [18,38], which block a substantial fraction of the beam current.

In this paper, we calculate optimized conditions for experiments with fourfold astigmatic beams as a function of Bragg scattering angle and acceleration voltage. Optimal values of $C_{3,4b}$, convergence, and collection angles are presented. A phase distribution for detection of in-plane magnetization is also presented. From an experimental perspective, the practical

considerations for setting up the desired value of fourfold astigmatism are described (Sec. V). A less patient reader or an experimentalist not interested into theoretical details may want to skip over the detailed description of the model (Secs. II, III, and IV A) and jump to the results of optimization, Secs. IV B–IV E, and practicalities of how to configure an aberrated electron probe, Sec. V.

II. INELASTIC SCATTERING OF CONVERGENT ELECTRON BEAMS

Here we describe the expressions for double-differential scattering cross section and mixed dynamical form factor, including the approximations used in the optimizations below.

A. Scattering cross section

A diffraction pattern with a transmitted beam with amplitude $T_{\mathbf{0}}$, and a set diffracted disks, each having an amplitude $T_{\mathbf{G}}$, is assumed. The implied $\mathbf{k}$ independence of $T_{\mathbf{G}}$ is a good approximation for a thin crystal. In addition, for thin samples the $T_{\mathbf{G}}$ is purely imaginary and its absolute value $|T_{\mathbf{G}\neq\mathbf{0}}| \ll 1$, while $T_{\mathbf{0}} \approx 1$. Using this notation, the elastically scattered wavefunction of the electron beam can be described as

$$\psi_{\text{in}}(\mathbf{r}) = \sum_{\substack{\mathbf{k},\mathbf{G} \\ k_\perp<\alpha/\lambda}} T_{\mathbf{G}} e^{i\chi_{\mathbf{k}}} e^{2\pi i(\mathbf{k}+\mathbf{G})\cdot\mathbf{r}}. \tag{1}$$

If the convergence semi-angle α is large enough, for certain $\mathbf{k}$ vectors also the $\mathbf{k}+\mathbf{G}$ vector may lie within the same disk. We note that to be consistent with the aberration function defined below, in this paper we use a convention with wavevector length $k = \frac{1}{\lambda}$. Thus a plane wave is given by expression $e^{2\pi i\mathbf{k}\cdot\mathbf{r}}$. The reciprocal-lattice vectors $\mathbf{G}$ are defined similarly by $e^{2\pi i\mathbf{G}\cdot\mathbf{R}} = 1$, where $\mathbf{R}$ are lattice vectors and, for instance, $|\mathbf{G}_{(100)}| = \frac{1}{a}$ for a cubic structure with lattice parameter a. This is therefore different from notation used in our previous publication, Ref. [32].

We remark here that the phase $\chi_{\mathbf{k}}$ may well reflect also the position of the probe over the sample in terms of a phase ramp $e^{2\pi i\mathbf{k}\cdot\Delta\mathbf{x}}$, which is nothing else than a phase contribution from the beam-shift "aberrations" $C_{0,1a}$ and $C_{0,1b}$, in Krivanek's notation [35].

Neglecting a constant prefactor, the double-differential scattering cross section can be expressed as [39]

$$\frac{\partial^2\sigma}{\partial E\partial\Omega} = \sum_{I,F} |\langle\psi_{\text{out}}| \otimes \langle F|\hat{V}|I\rangle \otimes |\psi_{\text{in}}\rangle|^2 \delta(E_F - E_I - E), \tag{2}$$

where $|I\rangle, |F\rangle$ are initial and final states of the sample, having energies E_I and E_F, respectively. E is the energy loss and $\hat{V}$ is the Coulomb interaction between electrons in the sample and the beam. The initial state probe wave function ψ_{in} is given in Eq. (1) and for the final-state wave function we will consider a single plane wave with wave vector $\mathbf{k}_f$, $\psi_{\text{out}} = e^{2\pi i\mathbf{k}_f\cdot\mathbf{r}}$, hitting a chosen pixel of the spectrometer camera. Plugging the wave functions in to Eq. (1) and following the same steps in deriving the scattering cross-section expression, as detailed in the Supplemental Material of Ref. [32], one arrives at the following expression:

$$\frac{\partial^2\sigma}{\partial E\partial\Omega} = \sum_{\substack{\mathbf{k},\mathbf{k}',\mathbf{G},\mathbf{G}' \\ k_\perp,k'_\perp<\alpha/\lambda}} T_{\mathbf{G}} T^{\star}_{\mathbf{G}'} e^{i(\chi_{\mathbf{k}}-\chi_{\mathbf{k}'})} S(\mathbf{q},\mathbf{q}',E), \tag{3}$$

where

$$\mathbf{q} = \mathbf{k}_f - \mathbf{k} - \mathbf{G}, \tag{4}$$

$$\mathbf{q}' = \mathbf{k}_f - \mathbf{k}' - \mathbf{G}'. \tag{5}$$

and $S(\mathbf{q},\mathbf{q}',E)$ is the mixed dynamical form factor [40] (MDFF) describing inelastic transitions.

B. Mixed dynamical form factor

The summation over initial and final states from Eq. (2) is contained in the MDFF:

$$S(\mathbf{q},\mathbf{q}',E) = \sum_{\tilde{I},F} \langle F|\frac{e^{-2\pi i\mathbf{q}\cdot(\mathbf{r}-\mathbf{u}_{\tilde{I}})}}{q^2}|\tilde{I}\rangle\langle\tilde{I}|\frac{e^{2\pi i\mathbf{q}'\cdot(\mathbf{r}-\mathbf{u}_{\tilde{I}})}}{q'^2}|F\rangle \times \delta(E - E_F + E_{\tilde{I}}), \tag{6}$$

where the summation over initial states $\tilde{I}$ is restricted over initial states of atoms within a unit cell (with basis vectors $\mathbf{u}_{\tilde{I}}$), instead of over the whole crystal. Thus, the summation over unit cells is already performed in Eq. (6), and results in an important condition for constructive interference, requiring the transversal (in-plane) component of $\mathbf{q}-\mathbf{q}'$ and therefore also $\mathbf{k}-\mathbf{k}'$ to be a reciprocal-lattice vector. We refer the reader to the Supplemental Information of Ref. [32] for more details.

In the numerical calculations below, there is only one atom per unit cell, located at the origin, i.e., basis vector $\mathbf{u} = 0$. Further, the MDFF is approximated by considering only dipole transitions [16]

$$S(\mathbf{q},\mathbf{q}',E) \approx \frac{1}{q^2q'^2}[\mathbf{q}\cdot\mathbb{N}(E)\cdot\mathbf{q}' + i(\mathbf{q}\times\mathbf{q}')\cdot\mathbf{M}(E)], \tag{7}$$

where $\mathbb{N}$ is, in general, a symmetric rank-2 tensor describing the distribution of charge and its anisotropy, and $\mathbf{M}$ is a vector containing information about spin and orbital magnetism and the magnetic dipole term. In general there are nine independent dipole contributions to the diffraction pattern: the three x,y,z components of the $\mathbf{M}(E)$ and six real components (xx,yy,zz,xy,xz,yz) of the tensor $\mathbb{N}(E)$ [16,41]. In the simplest case, if one assumes collinear magnetization along the z direction and a system with cubic symmetry, then $\mathbb{N}(E) \to N(E)\mathbb{1}$ and $\mathbf{M}(E) \to M(E)\hat{\mathbf{e}}_z$, i.e.,

$$S(\mathbf{q},\mathbf{q}',E) \approx \frac{1}{q^2q'^2}[N(E)\mathbf{q}\cdot\mathbf{q}' + i(q_xq'_y - q_yq'_x)M(E)]. \tag{8}$$

When the energy-loss spectrum is integrated over an energy edge (e.g., Fe $L_{2,3}$ edge), small changes of q_z, q'_z due to varying energy loss across the spectrum will be neglected. Similarly, the even smaller changes of dynamical Bloch coefficients across the edge interval with respect to energy loss will also be neglected. Under these assumptions, the dependence of edge-integrated MDFF on the electronic structure of a particular magnetic material is, up to a

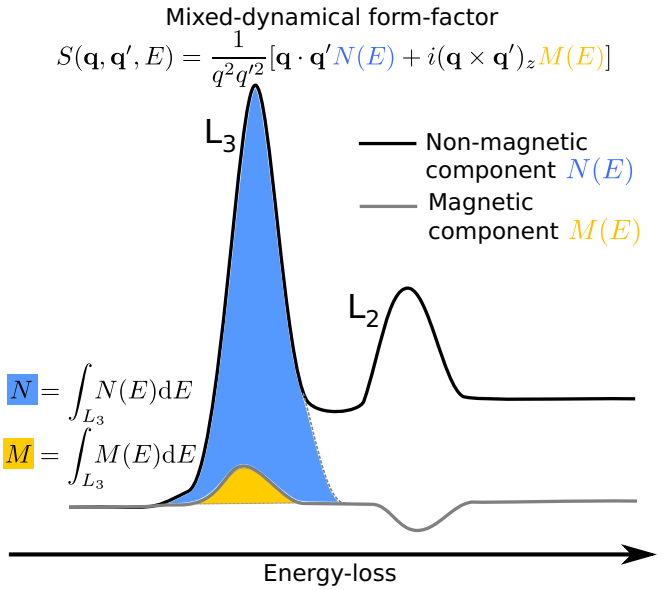

FIG. 1. Schematic picture of nonmagnetic and magnetic components of a mixed dynamical form-factor, $N(E)$ and $M(E)$, together with definition of L_3-edge integrated nonmagnetic and magnetic quantities, N and M, discussed in the text.

common scaling factor, determined by a single parameter—the ratio of magnetic and nonmagnetic component $M/N = \int M(E)dE/\int N(E)dE$. Figure 1 shows a typical shape of $N(E)$ and $M(E)$ for the case of $3d$ transition-metal $L_{2,3}$ edges, and the definition of their L_3-edge integrals N and M, respectively.

In this work we set the value of M/N to be equal to 1. This way the results presented below, such as maximal EMCD values (relative or absolute, or signal-to-noise ratios) become independent of a specific material. The actual absolute value of M/N depends on the sum-rules expressions [14–16], which connect the M/N to the details of the electronic structure of the studied material (for example, spin and orbital moments, number of holes in the $3d$-electron shell, strength of spin-orbital coupling, asphericity of the spin moment distribution, etc.)

The MDFF expression, Eq. (8), can be further simplified for the case of tetragonal or cubic symmetry, when noticing that an in-plane component of $\mathbf{q}-\mathbf{q}'$ must be a reciprocal-lattice vector $\mathbf{G}_\perp = \frac{1}{a}(m,n) \equiv a^\star(m,n)$ with m,n being integer Miller indices. In such case the real part of the MDFF can be written as

$$\mathrm{Re[MDFF]} \propto N\frac{\mathbf{q}.\mathbf{q}'}{q^2q'^2} = N\frac{q^2+(mq_x+nq_y)a^\star}{q^2q'^2}, \qquad (9)$$

the imaginary part of MDFF for magnetization along the z axis

$$\mathrm{Im[MDFF]} \propto \frac{(\mathbf{q}\times\mathbf{q}')_zM}{q^2q'^2} = Ma^\star\frac{nq_x-mq_y}{q^2q'^2}. \qquad (10)$$

For a magnetization along the x axis one obtains a rather compact expression

$$\mathrm{Im[MDFF]} \propto \frac{(\mathbf{q}\times\mathbf{q}')_xM}{q^2q'^2} = -\frac{Ma^\star nq_z}{q^2q'^2}, \qquad (11)$$

with its analog for y axis magnetization, where n gets replaced by the Miller index $-m$. The q'^2 in the denominator can of course be expressed as $q^2+2a^\star(mq_x+nq_y)+a^{\star2}(m^2+n^2)$, though that does not bring any additional insight and thus it was not used in the expressions above in order to keep them compact.

Equations (9)–(11) were used to express MDFF in Eq. (3) in all optimizations presented below.

C. EMCD signal

For clarity and completeness, we include here a short section defining the EMCD signal and its relation to the formalism used in this paper. First, within the approximations leading to Eqs. (3) and (8), we can write a general spectrum as a linear combination of the nonmagnetic component $N(E)$ and the magnetic component $M(E)$ of MDFF in the following way:

$$\begin{aligned}\frac{\partial^2\sigma}{\partial E\partial\Omega} &= \sum_{\substack{\mathbf{k},\mathbf{k}',\mathbf{G},\mathbf{G}'\\ k_\perp,k'_\perp<\alpha/\lambda}} T_\mathbf{G}T^\star_{\mathbf{G}'}e^{i(\chi_\mathbf{k}-\chi_{\mathbf{k}'})}\\ &\quad\times\frac{1}{q^2q'^2}[N(E)\mathbf{q}\cdot\mathbf{q}'+i(q_xq'_y-q_yq'_x)M(E)]\\ &= N(E)\sum_{\substack{\mathbf{k},\mathbf{k}',\mathbf{G},\mathbf{G}'\\ k_\perp,k'_\perp<\alpha/\lambda}} T_\mathbf{G}T^\star_{\mathbf{G}'}e^{i(\chi_\mathbf{k}-\chi_{\mathbf{k}'})}\frac{\mathbf{q}\cdot\mathbf{q}'}{q^2q'^2}\\ &\quad+M(E)\sum_{\substack{\mathbf{k},\mathbf{k}',\mathbf{G},\mathbf{G}'\\ k_\perp,k'_\perp<\alpha/\lambda}} iT_\mathbf{G}T^\star_{\mathbf{G}'}e^{i(\chi_\mathbf{k}-\chi_{\mathbf{k}'})}\frac{(\mathbf{q}\times\mathbf{q}')_z}{q^2q'^2}\\ &\equiv A(\Omega,\chi)N(E)+B(\Omega,\chi)M(E), \qquad (12)\end{aligned}$$

where $\mathbf{q},\mathbf{q}'$ are defined by Eqs. (4) and (5) in terms of $\mathbf{k}$, $\mathbf{k}'$, $\mathbf{G}$, and $\mathbf{G}'$. This naturally splits the spectrum into a nonmagnetic component $A(\Omega,\chi)N(E)$ and a magnetic component $B(\Omega,\chi)M(E)$. The latter term appears due to the magnetic dichroism and it is what we call EMCD. The terms A,B depend on the scattering angle Ω and the phase distribution of the incoming beam χ.

In a typical EMCD experiment we aim to acquire a pair of spectra with the following two properties: (1) that their nonmagnetic components are equal, i.e., $A_1 = A_2$, and (2) that their magnetic components have opposite sign: $B_1 = -B_2$. In a classical EMCD [3] experiment this is achieved by changing the position of the detector entrance aperture $\Omega_1 \to \Omega_2$, while in the approach described here we aim to do that by modification of the phase distribution of the incoming convergent beam $\chi_1 \to \chi_2$. As will be discussed below in Secs. III A and III B, this can be achieved for example by changing the sign of certain aberration coefficients. For completeness, we add that in an experiment with electron vortex beams [20], a suitable change of the phase distribution would be achieved by a change of sign, or chirality, of the initial orbital angular momentum of the beam.

Figure 2 shows an illustration of an EMCD experiment. The nonmagnetic component $A(\Omega,\chi)N(E)$ (NM) and the magnetic (EMCD) component $B(\Omega,\chi)M(E)$ are shown for a pair of spectra, which can be described as NM ± EMCD.

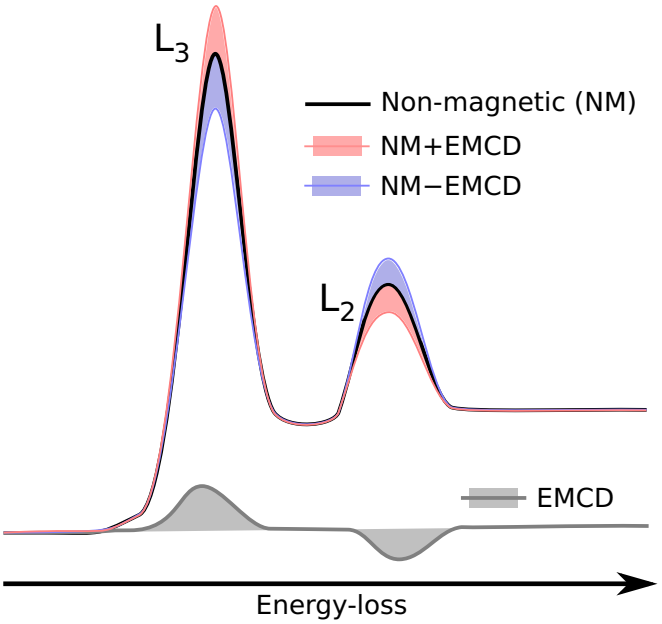

FIG. 2. Schematic picture of a pair of typical $L_{2,3}$ spectra for a $3d$ transition metal acquired in EMCD experiments (NM ± EMCD). They are separated into their nonmagnetic (NM) and magnetic (EMCD) components, respectively. NM and EMCD correspond to terms $A(\Omega,\chi)N(E)$ and $B(\Omega,\chi)M(E)$ of Eq. (12). Then the two spectra are given by $A(\Omega,\chi)N(E) \pm B(\Omega,\chi)M(E)$ for NM ± EMCD, respectively.

The EMCD signal is extracted from the difference of the two spectra.

Note that the difference of the two spectra in Fig. 2 actually leads to $2\times$ EMCD, following the definitions used in this paper. This is however of little importance, because the sum rule expression for the ratio of the orbital angular momentum and the spin angular momentum [14,15] is independent of the overall scale of the EMCD strength. In the literature one can see the relative strength of EMCD signal defined either as the difference of spectra divided by their sum, or as the difference of spectra divided by their average. Such percentages obviously differ by a factor of 2, nevertheless that has no influence on the extracted physical quantities.

In Sec. IV we will optimize the ratio of $B(\Omega,\chi)/A(\Omega,\chi)$ as a function of phase distribution χ, parametrized by aberration coefficients, as discussed in Sec. III.

III. PHASE DISTRIBUTION

The symmetry of the phase distribution plays a crucial role in detection of EMCD in spectrum imaging experiments, because the phase factor $e^{i(\chi_{\mathbf{k}}-\chi_{\mathbf{k}'})}$ can be tuned to maximize the intensity of the magnetic signal. We will discuss the symmetry requirements in the electron probe for both in-plane and out-of-plane magnetization orientations.

Generally, the phase distribution in the probe can be described by the so-called aberration function

$$\chi_{\mathbf{k}} = \frac{2\pi}{\lambda}\sum_{n,m}\frac{(k_\perp\lambda)^{n+1}}{n+1}(C_{n,ma}\cos m\theta + C_{n,mb}\sin m\theta), \quad (13)$$

where the $C_{n,ma}, C_{n,mb}$ are the aberration coefficients in Krivanek's notation [35]. The index n runs from zero to infinity and m is a non-negative integer, which runs from $n+1$ down in steps of 2. n denotes the order of the aberration and m its angular symmetry.

The angle θ is defined as $\arctan\frac{k_y}{k_x}$, $k_\perp = \sqrt{k_x^2+k_y^2}$ and $\lambda = \frac{hc}{\sqrt{2m_0c^2eV_{\mathrm{acc}}+(eV_{\mathrm{acc}})^2}}$ is the relativistically corrected de Broglie wavelength of incident electrons with m_0, e, c, h being electron mass and charge, speed of light and Planck's constant, respectively.

We note that the aberrations can also be expressed following Haider's notation, implemented in the CEOS aberration correctors [42]—i.e., second-order coma as B_2, threefold astigmatism as A_2, fourfold astigmatism as A_3, etc. In this work we follow Krivanek's notation because a casual reader, with a simple inspection of the aberration indexes (n,m), can understand the order and symmetry of the aberrations in the electron probe. It also simplifies the mathematical notation.

Today's (early 2016) state-of-the-art aberration correctors can manipulate aberrations up to the fifth order, $n=5$, and use them to partially compensate aberrations up to the seventh order [43].

Returning to Eq. (3), for each term with momentum transfer vectors $\mathbf{q},\mathbf{q}'$ there will be a term with a complex-conjugated prefactor having the pair of momentum transfer vectors swapped: $\mathbf{q}',\mathbf{q}$. Since the magnetic signal is carried by the imaginary part of the MDFF, Eqs. (10) and (11), the prefactors of MDFF in Eq. (3) need to have sizable imaginary parts. Considering that for very thin specimens $|T_{\mathbf{G}\neq 0}| \ll 1$ and $T_0 \approx 1$, the imaginary part can only originate from the phase factor. Denoting the phase difference $\Delta\chi_{\mathbf{k},\mathbf{k}'} = \chi_{\mathbf{k}} - \chi_{\mathbf{k}'}$, the summed contribution of the terms with $\mathbf{q},\mathbf{q}'$ and $\mathbf{q}',\mathbf{q}$, respectively, will be proportional to

$$\begin{aligned} &i(\mathbf{q}\times\mathbf{q}')\cdot\mathbf{M}e^{i\Delta\chi_{\mathbf{k},\mathbf{k}'}} + i(\mathbf{q}'\times\mathbf{q})\cdot\mathbf{M}e^{-i\Delta\chi_{\mathbf{k},\mathbf{k}'}} \\ &\quad = -2(\mathbf{q}\times\mathbf{q}')\cdot\mathbf{M}\sin\Delta\chi_{\mathbf{k},\mathbf{k}'} \end{aligned} \quad (14)$$

because $\Delta\chi_{\mathbf{k},\mathbf{k}'} = -\Delta\chi_{\mathbf{k}',\mathbf{k}}$. This is the key expression, from which one can derive suitable symmetry properties of phase distribution for detection of an EMCD signal in an EELS-STEM experiment.

A. In-plane magnetization

We start with the simpler case of in-plane magnetization. With magnetization along the x direction the scalar triple product is $(\mathbf{q}\times\mathbf{q}')\cdot\mathbf{M} = -Ma^\star nq_z \equiv -MG_yq_z$, according to Eq. (11). The q_z is mostly determined by energy loss, and the magnetization M is a material property that is not affected by electron diffraction. Thus the only variable in Eq. (11) is $G_y = na^\star$.

A cubic material is a good and simple illustrative case of what kind of aberrations are required to measure in-plane magnetization. In this case, a horizontal mirror axis (x axis) associates every term of the form given by Eq. (14) with its mirror image. The triple product changes sign, because $G_y \to -G_y$ under mirroring with respect to the x axis.

The main goal now is to tune the change of the phase factor, $\sin\Delta\chi_{\mathbf{k},\mathbf{k}'}$, in such a way that it maximizes the magnetic signal.

If the phase factor would be symmetric with respect to the x-mirror axis, then the magnetic signal would vanish thanks to the antisymmetry of the triple product. However, if one arranges the phase factor to be also antisymmetric with respect to the x axis, the magnetic signals add up instead of canceling each other out. Thus one concludes that the phase distribution should be such that $\Delta\chi_{\mathbf{k},\mathbf{k}'}$ is antisymmetric with respect to the x axis.

A similar analysis can also be done with the vertical mirror axis (y axis). In this case, the sign of the triple product does not change, because under the mirror y axis the G_y stays invariant. Following the same line of argumentation as above, one concludes that the phase difference $\Delta\chi_{\mathbf{k},\mathbf{k}'}$ has to be symmetric with respect to the y axis, such that the magnetic signals at each $\mathbf{k},\mathbf{k}'$ add up.

In summary, for a magnetization along the x axis, the optimal phase distribution should be such that the phase differences $\Delta_{\mathbf{k},\mathbf{k}'}$ are antisymmetric with respect to the x axis and symmetric with respect to the y axis. While there are infinitely many phase distributions fulfilling these conditions, there is also a particularly simple one among all of them: the lowest-order aberration $C_{0,1b}$—a simple beam shift:

$$\chi_{\mathbf{k}} = \frac{2\pi}{\lambda}\frac{(k_\perp\lambda)}{1}C_{0,1b}\sin(\theta) = 2\pi k_\perp C_{0,1b}\sin(\theta). \qquad (15)$$

Displacing the beam from an atomic column in the y direction up or down introduces a phase ramp in the $\mathbf{k}$-space disk of the beam wave function, which has the desired symmetry property; see Figs. 3(a) and 3(b).

Although here we have used the term "aberration," in practice one simply needs to acquire a standard STEM spectrum image with an aberration-corrected probe. The magnetic signal will be present in the spectrum image in pixels "above" and "under" the center of the atomic columns. This point is important because it implies that there already might be many experimental spectrum images published, where an atomically resolved magnetic signal is present but it has passed unnoticed. However, we advise the experimentalist to perform full dynamic electron-scattering calculations before claiming atomically resolved magnetic measurements from previous published data and in future experiments.

In the section below we optimize the probe displacements ($C_{0,1b}$) to find the distance at which the magnetic signal is the strongest; see Sec. IV D.

B. Out-of-plane magnetization

In the case of magnetization along the z axis, the triple product changes sign under all mirror axes: horizontal, vertical, and both diagonal ones (considering again a cubic crystal). That means that an optimal phase distribution should be such that the phase differences $\Delta\chi_{\mathbf{k},\mathbf{k}'}$ should be antisymmetric with respect to all of the mirror axes. Searching for a suitable solution among the aberrations $C_{n,m}$ gives fourfold astigmatism [32] $C_{3,4b}$ as the lowest-order aberration that satisfies the symmetry requirements. The resulting phase distribution is described by

$$\chi_{\mathbf{k}} = \frac{2\pi}{\lambda}\frac{(k_\perp\lambda)^4}{4}C_{3,4b}\sin(4\theta); \qquad (16)$$

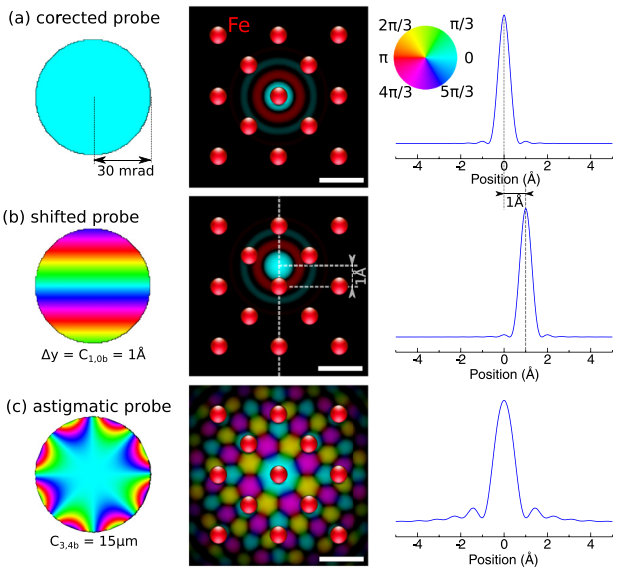

FIG. 3. Images of electron probes suitable for detection of in-plane and out-of-plane magnetization. Left column shows the $\mathbf{k}$-space wave function of the probe corresponding to convergence angle of $\alpha = 30$ mrad. The color represents phase according to the color wheel in the inset of the third column. The middle column shows the electron probe in real space in scale with the superposed atom positions of a bcc-iron structure. Hue represents phase and color brightness represents logarithm of probe intensity, the scale bar corresponds to 2 Å. The right column shows a radial profile (angular average) of the probe intensity. (a) Electron probe with all aberrations corrected, positioned on an Fe atomic column, (b) an identical aberration-corrected probe shifted by 1 Å along y direction, (c) probe with all aberrations corrected except for a fourfold astigmatism $C_{3,4b} = 15$ μm, centered on an Fe atomic column.

see also Fig. 3(c). Optimization of the conditions for measuring strong magnetic signals is the subject of the following Sec. IV.

We should note that the conditions derived above for the optimal symmetries of phase distribution are valid for a single term, like the one in Eq. (14). However, the inelastic scattering cross section is a sum over many such terms with a complicated interdependence. Thus, it is well possible that a phase distribution, which is globally optimal in terms of resulting magnetic signal strength, will not be perfectly symmetric or antisymmetric with respect to given mirror axes. This goes beyond the scope of this paper and is left for further investigation.

IV. OPTIMIZATION OF PHASES

In this section we describe our approach and results of optimization of the phase distribution. For a model diffraction pattern with fixed acceleration voltage and convergence angle, first the fourfold astigmatism is optimized as a function of lattice parameter. Next, the robustness of the magnetic signal with respect to residual aberrations is analyzed. The efficiency of beam shift is also studied in the detection of in-plane magnetization. Finally, for selected values of acceleration voltages the $C_{3,4b}$, convergence, and collection angles are optimized for maximal signal-to-noise ratio (SNR) in the experiments.

We should stress here that by the nature of our model, Eq. (3), the results shown below apply exactly only for an undistorted probe, i.e., the numerical values of EMCD strength should be valid only for very thin samples. For thicker samples the actual relative EMCD strength will be most likely reduced due to elastic scattering, channeling, and the resulting deformation of the probe. Only a full dynamical electron-scattering calculation, including elastic-scattering effects before and after the inelastic event, can provide a more reliable estimation of the EMCD strength. Yet, the model presented here should serve as a first-step qualitative guide for experimentalists and theoreticians in searching for magnetic signals in spectrum images.

A. Model diffraction pattern

Here we assume the case of a tetragonal crystal with crystal axes $a = b$ and a beam propagating along the c axis. In such a case, the four closest diffracted disks are at positions $(0, \pm a^\star)$ and $(\pm a^\star, 0)$. It is a matter of the relative size of α/λ and $a^\star$, whether the CBED disks overlap, and by how much.

To provide some actual numbers, at $V_{\mathrm{acc}} = 100$ kV, λ is 3.70 pm, and at $\alpha = 30$ mrad, the $\alpha/\lambda = 8.11$ nm^{-1} is comparable to $G_{(200)} = 2/a = 5.68$ nm^{-1} for fcc nickel with lattice parameter $a = 3.524$ Å. The corresponding twofold Bragg scattering angle is $2\Theta_B = \lambda G = 21$ mrad. This means that all five considered CBED disks overlap with each other; see Fig. 4. For a smaller convergence angle, one can prove that there are only overlaps of the transmitted beam with Bragg scattered beams. For the case of fcc Ni at 100 kV that happens if $\alpha < \lambda G/\sqrt{2} = \sqrt{2}\Theta_B = 14.8$ mrad. Eventually, there will be no overlap for $\alpha < G\lambda/2 = \Theta_B = 10.5$ mrad. All these diffraction situations are illustrated in Fig. 4.

The example of fcc Ni was chosen because it is a close-packed structure with relatively small interatomic distance. Fcc Ni also has quite a relative large number of kinematically forbidden reflections, i.e., its shortest kinematically allowed **G** vector is one of the longest ones among common crystal structures. In other words, in most of today's aberration-corrected STEMs there will be significant overlaps between the CBED disks, unless the convergence angle is deliberately chosen smaller than working at conditions offering the optimal spatial resolution.

The values of $V_{\mathrm{acc}} = 100$ kV and $\alpha = 30$ mrad were chosen, because these are typical operation conditions of the Nion UltraSTEM 100 electron microscope, to which we will refer in Sec. V.

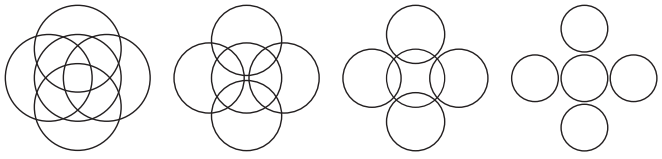

FIG. 4. Illustration of different degrees of overlap of the CBED disks as a function of relative sizes of convergence angle α and Bragg scattering angle Θ_B.

In the calculations below the **k** space was discretized at 2 pixels per mrad.

B. Optimization of fourfold astigmatism for magnetization along the optical axis (out of plane)

Here, the amplitude of diffracted beams $T_{\mathbf{G}}$ for $\mathbf{G} \neq 0$ is assumed to be negligible, i.e., $T_{\mathbf{G}} = 0$. This assumption is in principle fulfilled for very thin specimens, where the elastic-scattering effects on the probe shape are negligible. In such a case, the double-differential scattering cross section can be written using Eq. (3) as

$$\frac{\partial^2\sigma}{\partial E\,\partial\Omega} = \sum_{\substack{\mathbf{k},\mathbf{k}' \\ k_\perp, k'_\perp < \alpha/\lambda}} e^{i(\chi_{\mathbf{k}} - \chi_{\mathbf{k}'})} S(\mathbf{q}, \mathbf{q}', E). \tag{17}$$

The detector in the calculations is centered around the optical axis direction, $\mathbf{k}_f = (0,0,k_f)$. For a pointlike detection one can directly utilize the expressions Eqs. (9) and (10) to evaluate the nonmagnetic and magnetic signal, respectively, as a function of aberrations and a size of the reciprocal-lattice vector **G**. For a finite collection angle β there will be an additional summation over x, y components of $\mathbf{k}_f$, again discretized with a step of 0.5 mrad per pixel.

From the discussion in Sec. III, it is known that the phase differences $\Delta\chi_{\mathbf{k},\mathbf{G}} = \chi_{\mathbf{k}} - \chi_{\mathbf{k}+\mathbf{G}}$ should be antisymmetric with respect to all symmetry axes. In the calculated geometry, such condition is fulfilled by $C_{3,4b}$ and $C_{5,4b}$ aberrations. Because the latter one is much more difficult to manipulate in aberration-corrected STEMs available today (early 2016), the search was done for optimal values of $C_{3,4b}$ as a function of twofold Bragg scattering angle $2\Theta_B = \lambda G$. This is a simple optimization of a single parameter, which was performed by a direct evaluation of the relative strength of the EMCD signal for each pair of G and $C_{3,4b}$. The results are shown in Fig. 5 for various collection angles. The bottom panel of Fig. 5 shows also some typical examples of lengths of reciprocal-lattice vectors (vertical dashed lines), e.g., fcc nickel or (La/Sr)MnO_3 for illustration purposes.

Notice how the EMCD signal can change sign when $C_{3,4b}$ gradually increases at a fixed Θ_B. The actual optimal value of relative EMCD strength as a function of Θ_B is plotted in Fig. 6. As can be seen in Fig. 6, its behavior is not monotonic. The reasons for this behavior can be better understood from Fig. 5, where numerous lobes with an approximately hyperbolic shape can be observed. The lobes get denser towards small values of Θ_B. Moreover, at each constant Θ_B value there are numerous local minima, which results in a complicated deployment of numerical optimization routines. In principle, only a brute force search with a fine step, a long Monte Carlo simulation, or a simulated annealing with a slowly decreasing effective temperature would recover the global minimum.

At larger collection angles the optimized relative EMCD strength (Fig. 6) shows two broader local maxima. Increasing the collection angle also results in an EMCD signal decreasing in strength. Therefore, in actual experiments, a certain tradeoff must be found for the collection angle in order to optimize the magnetic SNR; see Sec. IV E.

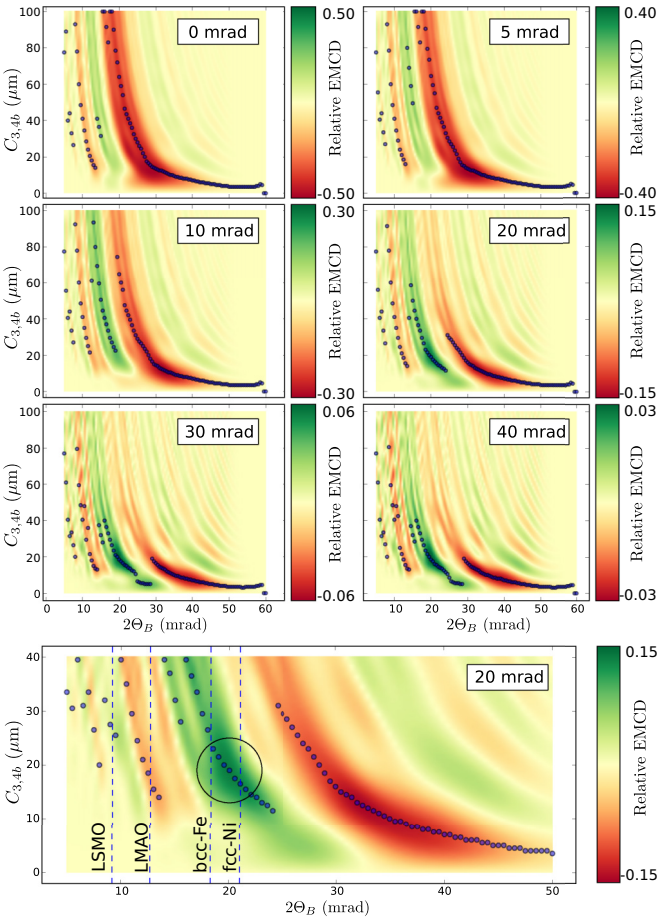

FIG. 5. Relative EMCD strength for out-of-plane magnetization for different collection angles as a function of $C_{3,4b}$ and twofold Bragg scattering angle $2\Theta_B$. The acceleration voltage is 100 kV and convergence semiangle 30 mrad. The collection angle is displayed in the legend of each plot. The blue dots mark the $C_{3,4b}$ values at which the absolute EMCD signal reaches its maximum for a given value of $2\Theta_B$. The vertical dashed lines in the bottom panel mark the Bragg scattering angles of (La/Sr)MnO_3, LaMnAOs, bcc-Fe, and fcc-Ni from left to right, respectively. Circle marks an optimal region, to which we refer in Sec. IV C.

C. Influence of residual aberrations for magnetization along the optical axis

An aberration corrector is designed to reduce the aberration coefficients under certain tolerable limits. In practice, some small nonzero values of aberrations are always present, but they can be compensated with lower-order aberrations of the same symmetry. For instance, a remaining $C_{5,2}$ aberration in the electron probe is compensated with $C_{3,2}$ and $C_{1,2}$ aberrations [43]. Thus a question arises of how sensitive is the expected EMCD strength with respect to other unwanted aberrations?

In the calculations below the same illumination conditions as in the previous sections are assumed ($\alpha = 30$ mrad, $V_{\rm acc} = 100$ kV). $C_{3,4b}$ and a collection angle β are set to 20 μm and 20 mrad, respectively, for the Bragg scattering angle of $\Theta_B = 20$ mrad. These electron optical conditions correspond to one of the optimal regions, marked with a black circle in Fig. 5,

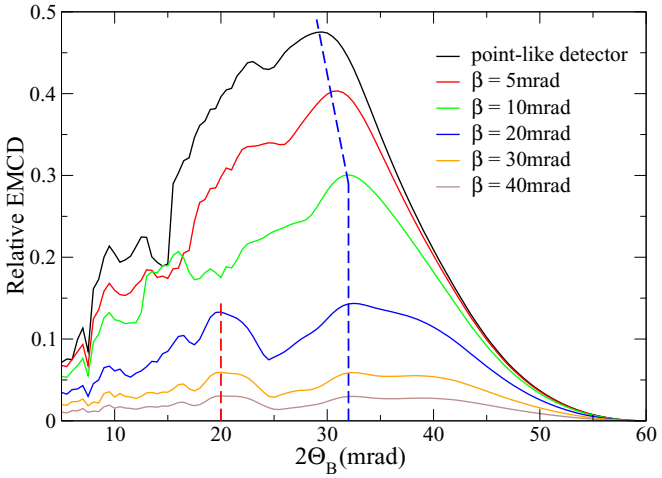

FIG. 6. Absolute value of the optimized relative EMCD strength, as a function of reciprocal-lattice vector represented by twofold Bragg scattering angle $2\Theta_B$ and collection angle β. The position of two local maxima is marked with dashed lines.

and where our idealized model predicts a relative EMCD strength of about 13% (at $N = M = 1$). The optimization was performed by searching for the limits when the relative EMCD strength is reduced by a factor of 2. The fourfold astigmatism value was fixed, while the other aberration coefficients, up to fifth order, were varied one by one.

The results are summarized in Table I. Some of the values deserve a few comments. First of all, the $C_{0,1}$ aberrations (beam shift) have limits of 0.23 Å, which means that the EMCD signal is rather strongly localized around the atom. This value should be compared to the diffraction-limited probe size, which has a full width at half maximum (FWHM) of 0.65 Å at $V_{\rm acc} = 100$ kV and $\alpha = 30$ mrad. In this context, the localization of the EMCD signal is about 2/3 of the electron probe FWHM.

The rotationally symmetric aberrations C_1, C_3, C_5 allow for quite non-negligible values. In particular, the spherical aberration (C_3 or C_s) can be up to ± 12 μm, which is more than a half of the desired fourfold astigmatism. Of course, reaching this value still requires an aberration corrector; nevertheless the optimum seems rather robust with respect to the value of spherical aberration. Interestingly, some of the even-m aberrations ($C_{1,2}, C_{5,6}$) have different limits for the a-type and

TABLE I. Robustness of the EMCD strength at $\alpha = 30$ mrad, $\beta = 20$ mrad, $V_{\rm acc} = 100$ kV, $\Theta_B = 20$ mrad with respect to parasitic aberrations. These values give limits above which the predicted EMCD strength is reduced by factor of 2 or more.

Aberration	Limits	Aberration	Limits
$C_{0,1ab}$	± 0.23 Å	$C_{4,1ab}$	± 0.28 mm
$C_1 = df$	± 8.4 nm	$C_{4,3ab}$	± 0.65 mm
$C_{1,2ab}$	$\pm 1.7/1.8$ nm	$C_{4,5ab}$	± 0.26 mm
$C_{2,1ab}$	± 110 nm	C_5	± 19 mm
$C_{2,3ab}$	± 270 nm	$C_{5,2ab}$	± 12 mm
$C_3 = C_s$	± 12 μm	$C_{5,4a}$	± 11.5 mm
$C_{3,2ab}$	± 5.6 μm	$C_{5,4b}$	$-16/+18$ mm
$C_{3,4ab}$	$\pm 5.4/7.5$ μm	$C_{5,6ab}$	$\pm 61/18$ mm

b-type aberrations. This is naturally the case also for $m = 4$ aberrations, where the influence of $C_{5,4b}$ is also asymmetric for positive vs negative values.

We notice that a well tuned Nion UltraSTEM 100 in a day-to-day performance has residual averaged values of fifth-order aberrations around 5 mm or smaller. The fourth-order residual aberrations are on average less than 200 μm, while the third-order residual aberrations are on average below 4 μm. We do not know the day-to-day performance of other aberration-corrected electron microscopes (i.e., FEI, JEOL, and Hitachi), but since their spatial resolutions are comparable at the same optical conditions, it is safe to assume that the residual aberrations are also similar. This means that under normal operational conditions an EMCD signal should be detected, in principle, in all aberration-corrected STEM, even in the presence of residual aberrations.

We summarize this subsection by noting that the EMCD signal should be well localized around the atomic column, and that it is relatively robust with respect to residual aberrations.

D. Optimization of beam shift for in-plane magnetization

Replacing the expression for magnetization along the z axis, Eq. (10), with an expression for magnetization along the x axis, Eq. (11), and using the same optimization routine described above, one can obtain maps of relative EMCD strength as a function of $C_{0,1b}$ and Bragg scattering angle.

For in-plane magnetization, the EMCD maps are very similar across all the considered collection angles (0, 5, 10, 20, 30, 40 mrad). Contrary to the magnetization along the z direction, the strength of the EMCD signal as a function of beam shift does not degrade strongly with the larger collection angles. Only a gradual smearing of the EMCD signal obtained for the pointlike detection is observed. For this reason, we show in Fig. 7 only the results for the pointlike detection ($\beta = 0$ mrad) and for the largest collection angle considered, $\beta = 40$ mrad. As expected, the dependence of beam shift reflects the periodicity of the crystal and dimension of the unit cell corresponding to the Bragg scattering angle.

These results indicate that if a TEM could achieve an atomic size probe in a Lorentz mode optical configuration, there should be a sizable magnetic signal, when the electron probe is displaced perpendicular to the direction of the magnetic moment. This effect could be also detected on strongly anisotropic magnetic materials, where the magnetization is kept in plane due to high magnetocrystalline anisotropy energy, despite the nonzero magnetic field of the objective lens, which is parallel to the optical axis.

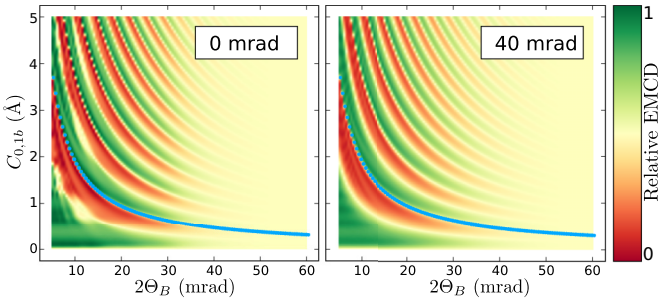

FIG. 7. Relative EMCD strength for in-plane magnetization as a function of $C_{0,1b}$ and twofold Bragg scattering angle $2\Theta_B$, calculated for 100-kV acceleration voltage and convergence semiangle 30 mrad. The collection angle is displayed in the legend of each plot. Blue dots mark the lattice parameter corresponding to Θ_B.

An optimum shift of approximately 0.2 Å appears to be almost independent of the Bragg scattering angle. Presumably, this is because the beam shape is fixed, while the calculations are performed across unit cells of different sizes. We notice that an electron probe shift by 0.2 Å in the opposite direction also produces the same EMCD signal but with opposite sign. Therefore in practice there might occur a quite strong cancellation of the positive and negative EMCD signals due to finite source size broadening.

We suggest that a larger probe (smaller convergence angle) will lead to a larger separation of the regions of positive and negative EMCD signal for in-plane magnetization, and therefore it will be more robust with respect to source size broadening.

E. Optimal signal-to-noise ratio of the EMCD signal

In this subsection we optimize the fourfold astigmatism, convergence, and collection angles for a range of lattice parameters a, with an effort to reach the highest magnetic SNR.

Definition of the magnetic signal is straightforward, since it is represented by the contribution from the imaginary parts of the MDFFs. However, the noise should be calculated from the total intensity at the core-level edges, which consists of the magnetic signal, nonmagnetic part originating from real parts of the MDFFs, but also from the background intensity following approximately a power law. The background contribution depends on a number of factors, for example the presence of other nearby edges, convergence, and collection angles, but also sample thickness. Many of these factors are well beyond the scope of our simple model. We will thus assume that the background intensity is approximately proportional to the nonmagnetic part of the edge signal intensity.

Next, we need to choose, how do we define the SNR. One could normalize the detection to a certain fixed number of counts, i.e., in an actual experiment that would mean waiting until a fixed total number of counts are accumulated at the desired edge. It is easy to show that SNR defined in this way would be proportional to a relative strength of the EMCD signal. This might sound reasonable on a first look, however, such optimization invariably leads to a preference of pointlike detection, because this is where the largest relative EMCD strengths are predicted; see Figs. 5 and 6. In practice this cannot be a viable solution, because a very small collection angle would mean long acquisition times and thus, most likely, also serious problems with beam damage and sample drift.

Both sample drift and beam damage constrain the acquisition time—so-called dwell time—and they do that in a different manner. Sample drift means a movement of the sample during the acquisition of the spectrum image, resulting in images that are distorted and warped. The operator of the microscope is then forced to limit the dwell time, so that the acquired images are interpretable. For experiments that are sample drift limited, one should seek to maximize the SNR per unit of acquisition time.

Achieving a maximum in the SNR per unit of acquisition time typically entails for a larger beam current ($I_p \propto \alpha^2$), and a larger collection angle β (integrated scattering cross-section is roughly proportional to β^2, when $\beta \lesssim \alpha$). Both aspects are naturally represented in our calculations and the definitions of $A(\Omega,\chi), B(\Omega,\chi)$; see Sec. II C and Fig. 2. Thus, normalizing the SNR to the detected counts per unit of time leads to a SNR expression that is proportional to the strength of the magnetic component divided by a square root of the nonmagnetic component of the EEL spectrum signal, i.e., SNR $\propto B/\sqrt{A}$.

For experiments when the beam damage is the primary factor constraining the dwell time, one should try to maximize the SNR per electron dose. Fixing the electron dose means that a product of A and acquisition time t is constant. SNR will be then proportional to $Bt/\sqrt{At} = \sqrt{t} \times B/\sqrt{A}$, i.e., $\sqrt{t}$ times the criterion for drift-limited optimization. The time to reach a given dose is inversely proportional to the beam current, which is itself proportional to squared convergence angle: $t \propto I_p^{-1} \propto \alpha^{-2}$. Finally, the quantity that we need to optimize becomes $1/\alpha \times B/\sqrt{A}$. This tends to favor smaller convergence angles and typically leads to higher relative strength of the EMCD signal, B/A.

Both optimization criteria have their own domain of suitability. Interestingly, very often they lead to the same results, especially in the case of small Bragg angles. In this section we present results for the SNR drift-limited experiment, but Tables II–V below in the Appendix summarize also the results for the dose-limited experiment.

For the optimization criteria one does not need actual SNR values; it is sufficient to optimize a property that is proportional to the SNR. On the other hand, with a suitable choice of various experimental parameters one could obtain semiquantitative estimates of the physical SNR. Those can give an experimentalist some idea about what levels of data counts are needed in order to detect a sufficiently strong EMCD signal.

The question is what parameters in an atomic resolved EMCD spectrum imaging experiment one needs to look out for semiquantitative estimates of the physical SNR?

The first obvious parameter is the number of pixels, N_{pix}, that an atomic column covers in the spectrum image. Other two straightforward parameters are the intensities of the background signal and the L-edge signal for each pixel. Since we are interested in detecting an EMCD signal, it is better to work with their total integrated intensities (or counts), i.e., C_{L_3} and C_{bkg}, for the L edge and background, respectively. Notice that here we work only with the L_3 peak, but the same concept applies to the L_2 peak.

Our experience in ORNL's Nion UltraSTEM 100 is that C_{L_3} and C_{bkg} can be in the order of thousand of counts for dwell times of few tens of milliseconds, and with atomic columns that cover $N_{\text{pix}} = 3 \times 3$ pixels. For simplicity we assume values of $C_{L_3} = 1000$ and $C_{bkg} = 2000$.

Another parameter to take into consideration is the ratio present between magnetic and nonmagnetic signals in the EEL spectra, M/N (see Sec. II B). The ratio M/N is limited by sum rules [14] due to the fact that the spin magnetic moment cannot be larger than the number of holes in the $3d$ shell. Assuming that the orbital moment is a small fraction of the spin moment and that the spin-orbital interaction is weak—both assumptions are typically well fulfilled for $3d$ materials—its maximum value for L_3 edge is $1/8 = 0.125$ (for the L_2 edge it is $1/4$). Here we assume $M/N = 0.1$, which is reasonable for $3d$ transition metals in their high-spin state.

Integrating the signal around an atomic column leads to a slight reduction of the relative strength of the EMCD, and so does source broadening. This effect can be taken into account by introducing a reduction factor f_{red}. For the example presented here $f_{\text{red}} = 0.8$.

With all these definitions, the optimized SNR simply becomes

$$\text{SNR} = \frac{|r_{\text{opt}}| f_{\text{red}} \frac{M}{N} N_{\text{pix}} C_{L_3}}{\sqrt{N_{\text{pix}}(C_{L_3} + C_{bkg})}} \approx 4.4|r_{\text{opt}}| \qquad (18)$$

per magnetic column, where r_{opt} is the ratio B/A found at optimum conditions. We should stress that although the resulting optimal SNR $\propto r_{\text{opt}}$, it is by no means true during the optimization procedure, as discussed above. This relation can be used only once the optimal conditions are found and the corresponding r_{opt} is extracted.

In the optimization of SNR, we have varied the Bragg scattering vectors from 5 to 25 mrad, which corresponds to lattice parameters a within a range 7.4–1.5 Å at 100 kV or 5.0–1.0 Å at 200 kV, respectively. The convergence angle was varied from 14 to 50 mrad and the collection angle was varied from 1 mrad up to the value of the convergence angle. This limit of collection angle was chosen because the simulations (Fig. 6) suggest that the relative strength of EMCD drops rapidly, once the collection angle approaches the value of the convergence angle. This restriction is also well supported *a posteriori* because none of the optimal solutions are at this boundary, i.e., having a collection angle equal to the convergence angle. Instead, the optimum collection angle is typically between 0.5α and 0.8α. For each combination of convergence and collection angles the value of $C_{3,4b}$ was varied from 0 to 40 μm with a step size of 0.5 μm.

Representative results of the optimization procedure are shown in Fig. 8 for twofold Bragg scattering angles of $2\Theta_B =$ 10, 15, and 20 mrad, respectively. One can see in the left column of Fig. 8 that the sign of the magnetic signal does not stay the same throughout the parameter space; instead it shows domains, within which it stays either positive or negative. This is related to the complicated topology of the magnetic signal dependence on $C_{3,4b}$, as seen in Fig. 5. The domains in Fig. 8 correlate with a qualitatively different range of values of optimized $C_{3,4b}$ shown in the middle column of Fig. 8. The resulting estimate of the SNR shown in the right column of Fig. 8 confirms the anticipated decrease of SNR for collection angles β approaching the values of convergence angle α, but primarily, there seems to be local optima of the SNR within each of the domains of EMCD sign.

As a function of the lattice parameter, with increasing lattice parameter (i.e., decreasing twofold Bragg scattering angle $2\Theta_B$) the domains seem to systematically shrink and move down and left towards smaller convergence and collection angles. This indicates that the preferred beam sizes approximately scale with the lattice parameter. Along with the shrinking of domains, the peak SNR within these domains is fading to smaller values, giving space to new

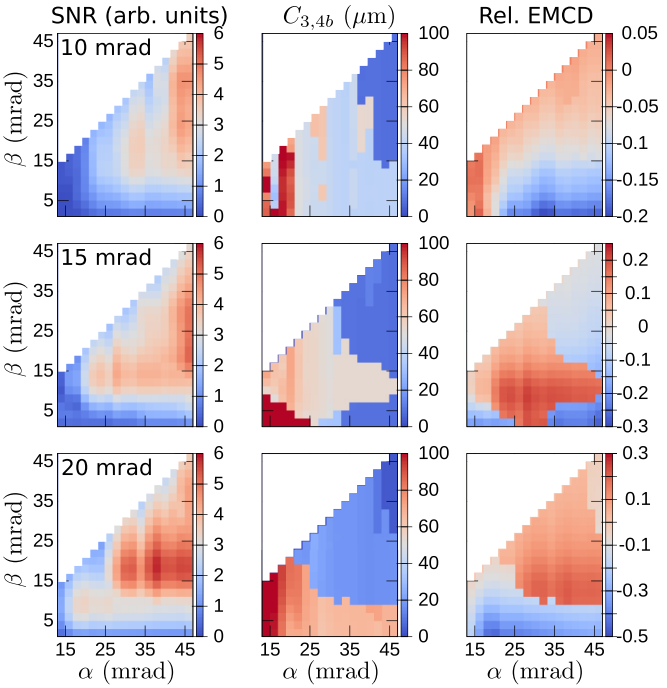

FIG. 8. Optimization of the magnetic SNR for Fe-L_3 edge at $V_{\mathrm{acc}} = 100$ kV for a structure with twofold Bragg scattering angle $2\Theta_B = 10$ mrad (top), 15 mrad (middle row), 20 mrad (bottom), i.e., $a = 3.70$, 2.47, and 1.85 Å, respectively. For each combination of convergence angle α and collection angle $\beta < \alpha$ the highest SNR (in arbitrary units; left column) obtained for optimal $C_{3,4b}$ value (middle column) and the resulting relative strength of the EMCD signal (right column) are plotted. Values where $\beta > \alpha$ were not calculated (white color).

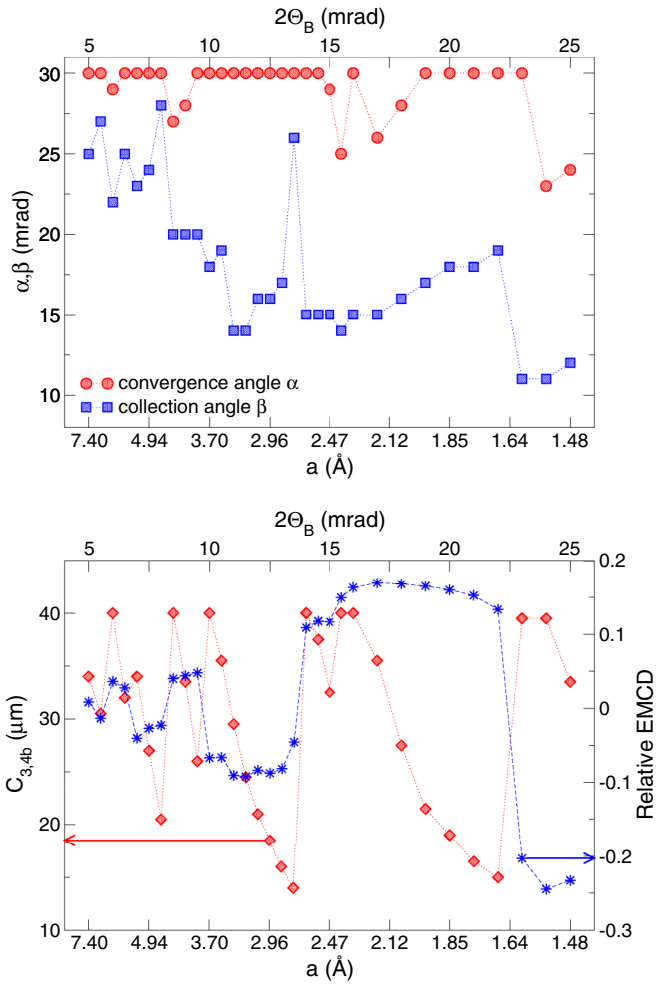

FIG. 9. Summary of optimized settings for Fe-L_3 edge at $V_{\mathrm{acc}} = 100$ kV as a function of twofold Bragg scattering angle $2\Theta_B$ or lattice parameter a, respectively. Convergence and collection angles are shown in the top panel and the desired fourfold astigmatism $C_{3,4b}$ and resulting relative strength of EMCD signal are shown in the bottom panel. The convergence angle α was restricted to a maximum of 30 mrad in these plots.

domains appearing at larger convergence/collection angles and eventually offering higher SNR. It seems likely that when larger convergence/collection angles can be used, there will be more domains with alternating positive and negative signs of the EMCD signal strength, and possibly with rising SNR.

A summary of the optimization results over the whole range of Bragg scattering angles is presented in Fig. 9. The actual extracted optimum depends on the maximum convergence angle achievable in an electron microscope. Therefore for practical purposes, we show here results for maximum convergence angles 30 mrad suitable for the Nion UltraSTEM 100 electron microscope.

The optimal convergence angle is often located at the boundary of 30 mrad, suggesting that if larger convergence angles would be achievable, the SNR could be further improved. The collection angle is varying between 11 and 28 mrad. In dependence of $C_{3,4b}$ on $2\Theta_B$ one can identify a set of monotonous segments, followed by a sudden change of the value. These segments are related to the domains in Fig. 8 and their changes with respect to Θ_B discussed above. The $C_{3,4b}$ values fall into the range 14–40 μm.

The plots in Fig. 9 constitute one of the primary outcomes of this paper. Actual numerical values are summarized in Tables II–V in the Appendix.

Returning to the question of feasibility of the experiment, let us shortly discuss the estimate of SNR as given by Eq. (18). From Fig. 9 and the tables below one can see than a value of $r_{\mathrm{opt}} \gtrsim 0.10$ should be reachable for most, except for the largest of the column spacings. Equation (18) then gives SNR of $\sim$0.44 per magnetic column, which means that for the electron counts estimated above, the EMCD signal would be covered by noise. To reach SNR ≈ 3 we would need to either collect a signal from approximately 7×7 magnetic columns, which is an area of approximate extent 1–4 nm^2, or we would need to increase the electron counts C_{L_3} by a longer dwell time and/or finer scanning step allowing us to use higher N_{pix}. We remind that our optimization refers to thin samples. For thick samples (tens of nanometers) the relative strength of the EMCD signal should drop significantly.

In classical EMCD geometries based on two-beam or three-beam orientations [3,4,9] probe sizes close to 1 nm have been already reached, yet the EMCD on a pixel-by-pixel basis is still rather noisy. However, with atomic size probes one can freely decide the shape of the scanned area, e.g., a thin stripe parallel to a surface or an interface. In addition, the atomic

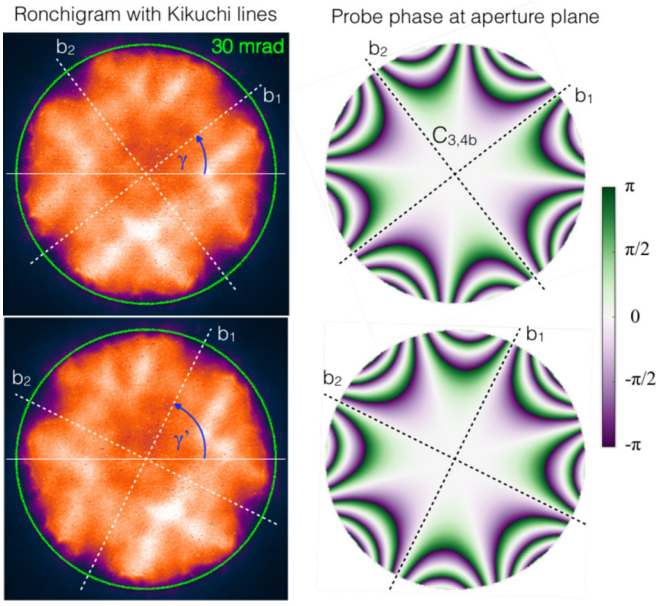

FIG. 10. Schematic of Ronchigrams of a LaMnAsO grain oriented along the c axis, and phase distributions of fourfold astigmatism probes at the aperture plane. The Ronchigram in the bottom is a copy of the top panel that has been digitally rotated after acquisition for illustration purposes.

size of the probes allows us to detect an EMCD signal also from antiferromagnetic compounds, which is not possible with probes larger than a unit cell.

V. CREATING A $C_{3,4}$ ABERRATED PROBE

As it was shown in Sec. III B, a $C_{3,4}$ aberrated probe is needed in order to achieve an effective EMCD signal when performing STEM spectrum imaging experiments. However, it is not enough to only add an absolute value of $C_{3,4}$ aberration in the electron probe. The electron probe when entering the sample also has to have an antisymmetric phase distribution with respect to the main axes of the sample. In other words, the $C_{3,4b}$ aberration, which is antisymmetric about the principal longitudinal plane of the corrector (because of its $\sin 4\theta$ angular dependence), has to be aligned with the main axes of the sample. Figure 10 shows schematically how the phase distribution of the $C_{3,4b}$ aberration is antisymmetrically aligned with the main axes of a crystalline sample. Note the Kikuchi lines in the Ronchigrams (left column) parallel to crystal axes b_1 and b_2 and the desired phase distribution (right column).

However, it is very unlikely that the sample is loaded in a TEM holder, such that after being tilted to zone axis, both axes, sample and corrector, coincide. Thus, in practice the proper amount of $C_{3,4a}$ and $C_{3,4b}$ aberrations need to be added to produce a $C_{3,4}$ phase distribution that is antisymmetrically aligned with the sample main axes of the sample.

The first step to produce a correct $C_{3,4b}$ phase distribution on the electron probe is to measure the relative alignment of the corrector longitudinal axes with the horizontal axis. For instance, one method is selecting a recognizable feature in the sample when imaged with the Ronchigram camera. Observe how that feature shifts, using a relative large defocus of -1000 nm, with a beam shift of few tens of nm along the a axis of the corrector. The relative angle is obtained by tracing a line from the initial to the final position of the selected feature, and measuring the angle that the line has with the horizontal axis. Another approach is to select a feature while imaging the sample in STEM mode, with the scanning coils relative rotation set to zero, then proceed to perform a beam shift along the a axis of the corrector, and measure the relative angle of the line formed by the shifted feature and the horizontal axis. This last approach also requires one to know the relative angle between the axes of the Ronchigram camera and the axes of the scanning coils.

The next step requires one to obtain the relative angle between the main axes of the sample with the horizontal axis. This can be achieved by identifying a main Kikuchi line of the crystalline sample, which previously has been aligned in a main zone axis, and measuring its relative angle with the horizontal axis. Usually an illumination of the sample in STEM mode with a defocused electron probe (500–1000 nm) is enough to resolve the Kikuchi lines of a crystalline sample.

Notice that the sample here has to have a tetragonal symmetry after being aligned in the major zone axis of interest. As a consequence, pairs of Kikuchi lines with different spacing could be observed, depending on the lattice parameters of the sample. It is not important which Kikuchi line is selected in this case. One can select the line that has the smallest angle with respect to the horizontal axis. However, the relative angles of both the corrector and the sample with the horizontal axis need to be defined consistently (either clockwise or counterclockwise).

The desired phase distribution of the aberrated electron probe is obtained by calculating the amount of $C_{3,4a}$ and $C_{3,4b}$, as $C_{3,4a} = C_{3,4}\cos\delta$ and $C_{3,4b} = C_{3,4}\sin\delta$. Here, δ is the difference of the relative angles between the sample and the corrector with the horizontal axis.

Finally, the values of $C_{3,4a}$ and $C_{3,4b}$ aberrations need to be used in the aberration correction algorithm, such that the lenses in the corrector produce the desired phase distribution. In a Nion microscope, this is achieved by selecting as $C_{3,4a}$ and $C_{3,4b}$ target values the new calculated $C_{3,4}$ aberrations. Then one simply needs to proceed with the aberration correction algorithm as in a normal operation procedure [35]. The desired $C_{3,4}$ aberrated probe is normally reached within a few minutes.

Figure 10 shows two schematic examples of a LaMnAsO grain that has been aligned such that its c axis is parallel to the electron-beam direction. The grain is shown with two different relative angles between its respective Kikuchi lines and the horizontal axis. If the relative angle of the corrector with the Ronchigram camera is zero, then for the two schematic examples shown in Fig. 10, $\delta = \gamma$ and $\delta = \gamma'$.

Figure 11 shows simulated Ronchigrams of an amorphous sample illuminated with electron probes with 15 μm of $C_{3,4a}$ (top row) and $C_{3,4b}$ (bottom row) aberrations. The fourfold symmetry of the $C_{3,4}$ aberration can be appreciated in the Ronchigram for relatively large defocus values of ± 20 nm. Additionally, the relative rotation of 22.5° between the $C_{3,4a}$ and $C_{3,4b}$ aberrations can be observed by the rotation of the fourfold features in the Ronchigram. However, it looks like if at opposite defocus values of 20 and -20 nm the fourfold features observed in the Ronchigram also rotate, in this case by 45°.

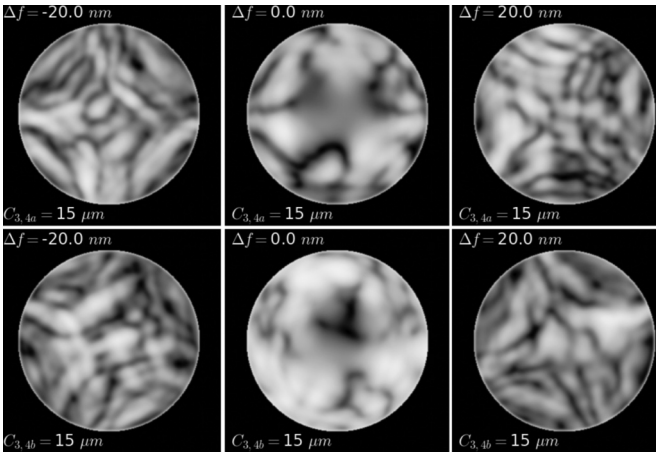

FIG. 11. Simulated Ronchigrams of an amorphous sample illuminated with a $C_{3,4}$ aberrated electron probe. The simulations were performed for 100-kV acceleration voltage and convergence semiangle of 30 mrad. The a axis of the corrector is parallel to the horizontal axis.

The apparent rotation is due to an enhancement of the negative lobes of the $C_{3,4}$ aberrations (a and b) for a negative defocus value, while for a positive defocus value the enhancement occurs in the positive lobes of the $C_{3,4}$ aberrations. This effect is better appreciated if only the phase of a $C_{3,4}$ probe is plotted at the aperture plane, as shown in Fig. 12.

Figure 13 shows experimental Ronchigrams of an amorphous carbon film illuminated with a $C_{3,4}$ aberrated probe. Similarly as in the case of the simulation, the fourfold symmetry features of the $C_{3,4}$ aberration and their apparent rotation for opposite defocus values can be observed in the Ronchigram. The dashed red lines at a defocus value of -20 nm show the relative rotation of the fourfold features in the Ronchigrams.

Our experience in setting a $C_{3,4}$ aberrated probe indicates that the alignment of the effective $C_{3,4b}$ phase distribution can be achieved within $\sim 3^\circ$ of the desired rotation. For a 15-μm $C_{3,4}$ probe that means less than 1 μm of a residual $C_{3,4}$, which is within the limits of $C_{3,4a}$ and $C_{3,4b}$ aberrations required for the EMCD measurements (see Table I). The estimate in the accuracy of the measurements has been obtained by comparing the measured values of $C_{3,4a}$ and $C_{3,4b}$

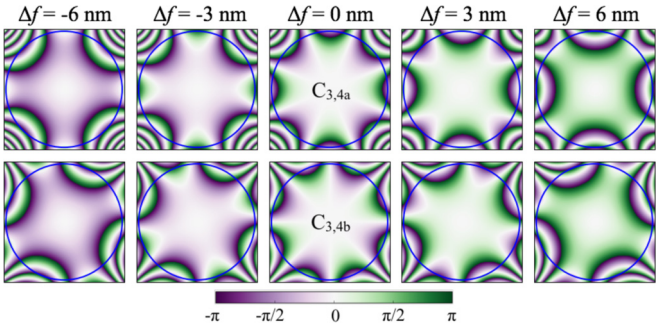

FIG. 12. Phase distribution at the aperture plane of 15 μm of $C_{3,4a}$ and $C_{3,4b}$ aberrations as a function of defocus Δf. The simulations were performed for 100-kV acceleration voltage. The blue circle schematically highlights the convergence semiangle of 30 mrad.

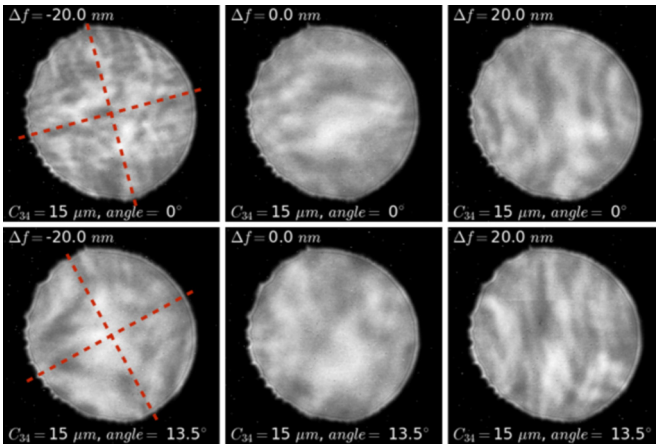

FIG. 13. Experimental Ronchigrams of an amorphous sample illuminated with a $C_{3,4}$ aberrated electron probe. The experiments were performed for 100-kV acceleration voltage and convergence semiangle of 30 mrad. The experiments were performed by configuring the corrector such that the $C_{3,4a}$ and $C_{3,4b}$ aberrations generate a relative rotation of the fourfold features in the Ronchigrams. The relative rotation angle is shown for each row.

with their desired target values. The procedure was carried out at different rotations of the $C_{3,4}$ phase distribution with respect to the longitudinal plane of the corrector.

VI. CONCLUSIONS AND OUTLOOK

We have described in detail an approach to atomic resolution measurement of magnetic properties based on an EMCD method using aberrated electron probes. Model of inelastic scattering of a convergent electron probe provides a simple explanation of the desired symmetries of the probe phase distribution. Within the model, the key experimental parameters—strength of fourfold astigmatism, convergence, and collection angles—have been optimized to achieve the strongest signal-to-noise ratio. Finally, the actual procedure of setting the fourfold astigmatism in experiments has been discussed.

Based on the results of optimization of signal-to-noise ratio, it appears that one could profit from the new generation of aberration correctors allowing one to use larger convergence angles, at least for very thin samples.

When discussing the symmetry considerations that an electron probe has to have in its phase distribution for EMCD measurements, one needs to distinguish between necessary and sufficient conditions. The perfect antisymmetry of phase distribution is a sufficient condition for observing atomic resolution EMCD, but strictly speaking it is not necessary. This opens for a possibility that less symmetric probes utilizing several types of aberrations at once might provide more optimal probes. This is at present under investigation and will be the subject of another publication.

Another direction of further optimization of the probe is based on an observation that a substantial part of the fourfold astigmatic probe wave function in the **k** space—the middle section—has a negligible phase variation. As a consequence, the center of the electron probe is inactive in the generation of the needed phase distribution for detection of an EMCD

signal. Using an annular aperture with a carefully chosen inner and outer radii, instead of a circular one, will partially reduce the center part of the electron probe and enhance its tails in real space with the required phase distribution. An electron probe formed with an annular aperture should increase the relative strength of the EMCD signal without sacrificing too much SNR.

Finally, in this work we have focused on the detection of magnetic properties in materials. However, one could well imagine that electron probe shapes could be tailored to detect other materials properties with unprecedented spatial resolution, such as charge ordering, crystal-field splitting, spin-orbit-coupling, optical dichroism, and other physical phenomena associated with broken symmetries such as topological insulators and quantum Hall effect.

All these outlined directions call for further research in a different class of electron energy-loss spectroscopy experiments—experiments where aberration correctors and shaped apertures in STEM will be used, not only to achieve the smallest possible probes, but instead, to sculpt the electron wave function such that its phase distribution could be harvested at will to reveal interesting physical phenomena.

ACKNOWLEDGMENTS

J.R. acknowledges Swedish Research Council, STINT and Göran Gustafsson's Foundation. J.-C.I. acknowledges support by ORNL's Center for Nanophase Materials Sciences (CNMS), which is a U.S. Department of Energy, Office of Science User Facility.

APPENDIX: SUMMARY OF OPTIMIZED PARAMETER VALUES FOR EMCD EXPERIMENTS WITH FOURFOLD ASTIGMATIC PROBES

In this appendix we summarize the numerical values of optimized parameters for convergence and collection angles and fourfold astigmatism, as a function of lattice parameter (or twofold Bragg angle). Individual tables show results for two values of maximal convergence angle, 30 or 50 mrad, and for two values of acceleration voltage, 100 and 200 kV.

The optimization procedure and ranges of parameter values are described in the text, Sec. IV E. As mentioned in the

TABLE II. Optimized convergence angle α, collection angle β, and fourfold astigmatism $C_{3,4b}$ for EMCD measurements at Fe L_3 edge of cubic or tetragonal structures with magnetization along the c axis and parallel to electron beam. Acceleration voltage 100 kV, maximum convergence angle 30 mrad.

$2\Theta_B$ (mrad)	a (Å)	α (mrad)	β (mrad)	$C_{3,4b}$ (μm)	Relative EMCD, r_{opt}
5.0	7.40	30	25	34.0	0.008
5.5	6.73	30	27	30.5	−0.014
6.0	6.17	29	22	40.0	0.036
6.5	5.70	30	25	32.0	0.028
7.0	5.29	30	23	34.0	−0.040
7.5	4.93	30 (29)	24 (26)	27.0 (25.5)	–0.027 (–0.025)
8.0	4.63	30	28	20.5	−0.023
8.5	4.36	27	20	40.0	0.040
9.0	4.11	28	20	33.5	0.044
9.5	3.90	30	20	26.0	0.048
10.0	3.70	30	18	40.0	−0.067
10.5	3.52	30	19	35.5	−0.066
11.0	3.37	30 (27)	14 (14)	29.5 (31.0)	–0.091 (–0.086)
11.5	3.22	30 (28)	14 (14)	24.5 (26.0)	–0.092 (–0.092)
12.0	3.08	30	16	21.0	−0.084
12.5	2.96	30	16	18.5	−0.088
13.0	2.85	30	17	16.0	−0.082
13.5	2.74	30	26	14.0	−0.045
14.0	2.64	30	15	40.0	0.109
14.5	2.55	30 (28)	15 (14)	37.5 (37.5)	0.118 (0.123)
15.0	2.47	29 (24)	15 (14)	32.5 (40.0)	0.117 (0.126)
15.5	2.39	25	14	40.0	0.150
16.0	2.31	30 (25)	15 (15)	40.0 (40.0)	0.163 (0.156)
17.0	2.18	26	15	35.5	0.170
18.0	2.06	28	16	27.5	0.168
19.0	1.95	30 (29)	17 (17)	21.5 (23.0)	0.165 (0.166)
20.0	1.85	30	18	19.0	0.160
21.0	1.76	30	18	16.5	0.153
22.0	1.68	30	19	15.0	0.134
23.0	1.61	30 (22)	11 (10)	39.5 (40.0)	–0.203 (–0.244)
24.0	1.54	23 (22)	11 (11)	39.5 (40.0)	–0.245 (–0.239)
25.0	1.48	24 (23)	12 (11)	33.5 (35.0)	–0.233 (–0.249)

TABLE III. The same as Table II, with $V_{\text{acc}} = 200$ kV.

$2\Theta_B$ (mrad)	a (Å)	α (mrad)	β (mrad)	$C_{3,4b}$ (μm)	Relative EMCD, r_{opt}
5.0	5.02	29	24	31.0	−0.020
5.5	4.56	28	20	39.5	0.042
6.0	4.18	29	22	27.5	0.038
6.5	3.86	29	23	31.0	−0.041
7.0	3.58	30	24	23.0	−0.039
7.5	3.34	29	26	17.5	−0.027
8.0	3.13	25	16	36.5	0.055
8.5	2.95	27	17	27.0	0.053
9.0	2.79	30	12	40.0	−0.120
9.5	2.64	30	12	33.0	−0.136
10.0	2.51	30	12	28.0	−0.130
10.5	2.39	30 (26)	13 (13)	23.5 (24.5)	–0.113 (–0.102)
11.0	2.28	30 (27)	13 (13)	20.0 (20.5)	–0.115 (–0.109)
11.5	2.18	30 (28)	14 (14)	16.5 (17.5)	–0.107 (–0.105)
12.0	2.09	30	14	14.5	−0.114
12.5	2.01	30	15	12.5	−0.106
13.0	1.93	27	13	39.0	0.123
13.5	1.86	28 (22)	13 (13)	33.5 (40.0)	0.128 (0.116)
14.0	1.79	29 (22)	14 (13)	29.0 (40.0)	0.121 (0.136)
14.5	1.73	28 (23)	13 (13)	40.0 (40.0)	0.159 (0.155)
15.0	1.67	28 (23)	14 (13)	35.5 (39.5)	0.156 (0.163)
15.5	1.62	29 (24)	14 (14)	31.5 (34.0)	0.160 (0.155)
16.0	1.57	30 (25)	15 (14)	27.5 (29.5)	0.153 (0.161)
17.0	1.47	27 (26)	15 (15)	22.5 (24.0)	0.155 (0.156)
18.0	1.39	28	16	18.5	0.154
19.0	1.32	30 (29)	17 (17)	14.5 (15.5)	0.150 (0.150)
20.0	1.25	30	17	13.0	0.153
21.0	1.19	30 (20)	18 (9)	11.5 (40.0)	0.135 (−0.227)
22.0	1.14	30 (20)	19 (10)	10.0 (40.0)	0.117 (−0.209)
23.0	1.09	22 (21)	11 (10)	31.5 (33.0)	–0.201 (–0.216)
24.0	1.04	23 (22)	11 (11)	26.5 (28.0)	–0.208 (–0.203)
25.0	1.00	24 (23)	12 (11)	22.5 (23.5)	–0.197 (–0.211)

TABLE IV. The same as Table II, but with maximum convergence angle $\alpha = 50$ mrad.

$2\Theta_B$ (mrad)	a (Å)	α (mrad)	β (mrad)	$C_{3,4b}$ (μm)	Relative EMCD, r_{opt}
5.0	7.40	50	37	16.0	0.022
5.5	6.73	46	40	11.0	0.018
6.0	6.17	50 (31)	45 (22)	8.0 (40.0)	0.017 (0.041)
6.5	5.70	34	25	29.0	0.040
7.0	5.29	36	26	22.0	0.041
7.5	4.93	39	28	16.5	0.041
8.0	4.63	41	29	13.0	0.042
8.5	4.36	44	32	10.0	0.042
9.0	4.11	46	33	8.0	0.042
9.5	3.90	49	34	6.5	0.044
10.0	3.70	48 (32)	35 (19)	8.0 (39.5)	−0.043 (–0.075)
10.5	3.52	50 (33)	39 (19)	4.5 (33.0)	0.037 (−0.082)
11.0	3.37	49 (35)	38 (21)	5.5 (27.0)	−0.043 (–0.076)
11.5	3.22	50 (36)	26 (21)	4.5 (23.0)	−0.061 (–0.080)
12.0	3.08	50 (38)	41 (23)	4.0 (19.0)	−0.036 (–0.077)
12.5	2.96	42 (39)	24 (24)	16.0 (16.5)	−0.077 (–0.076)
13.0	2.85	41	24	14.0	−0.081
13.5	2.74	45 (43)	27 (18)	12.0 (12.0)	−0.074 (–0.121)
14.0	2.64	44	19	10.5	−0.120
14.5	2.55	46	19	9.0	−0.127
15.0	2.47	47 (24)	19 (14)	8.0 (40.0)	−0.133 (0.126)
15.5	2.39	49 (25)	21 (14)	7.0 (40.0)	−0.121 (0.150)
16.0	2.31	50 (25)	21 (15)	6.0 (40.0)	−0.123 (0.156)
17.0	2.18	50 (26)	21 (15)	5.0 (35.5)	−0.120 (0.170)
18.0	2.06	34 (28)	17 (16)	25.0 (27.5)	0.161 (0.168)
19.0	1.95	36 (29)	17 (17)	20.5 (23.0)	0.171 (0.166)
20.0	1.85	38 (31)	18 (18)	16.5 (18.0)	0.169 (0.165)
21.0	1.76	40 (32)	20 (19)	13.5 (15.5)	0.158 (0.161)
22.0	1.68	41 (34)	20 (20)	11.5 (12.5)	0.166 (0.162)
23.0	1.61	43 (35)	21 (20)	9.5 (10.5)	0.164 (0.168)
24.0	1.54	45 (22)	22 (11)	8.0 (40.0)	0.163 (−0.239)
25.0	1.48	47 (23)	23 (11)	7.0 (35.0)	0.158 (−0.249)

TABLE V. The same as Table III, but with maximum convergence angle $\alpha = 50$ mrad.

$2\Theta_B$ (mrad)	a (Å)	α (mrad)	β (mrad)	$C_{3,4b}$ (μm)	Relative EMCD, r_{opt}
5.0	5.02	50	38	11.0	0.024
5.5	4.56	46 (28)	42 (20)	7.5 (39.5)	0.018 (0.042)
6.0	4.18	44 (31)	26 (22)	30.0 (27.5)	0.038 (0.043)
6.5	3.86	34	23	19.5	0.044
7.0	3.58	36	25	15.0	0.044
7.5	3.34	39	27	11.0	0.044
8.0	3.13	42 (38)	28 (28)	8.5 (13.5)	0.043 (−0.045)
8.5	2.95	44 (38)	30 (30)	7.0 (10.5)	0.042 (−0.043)
9.0	2.79	46	32	5.5	0.044
9.5	2.64	49 (30)	33 (12)	4.5 (33.0)	0.044 (−0.136)
10.0	2.51	48 (31)	35 (13)	5.5 (27.5)	−0.044 (–0.126)
10.5	2.39	50 (33)	37 (13)	4.5 (22.5)	−0.044 (–0.141)
11.0	2.28	50 (35)	24 (14)	3.5 (18.5)	−0.067 (–0.135)
11.5	2.18	50 (36)	26 (14)	3.0 (15.5)	−0.065 (–0.144)
12.0	2.09	38	15	13.0	−0.141
12.5	2.01	42 (39)	16 (16)	11.0 (11.0)	−0.134 (–0.133)
13.0	1.93	41	16	9.5	−0.146
13.5	1.86	43 (22)	17 (13)	8.0 (40.0)	−0.139 (0.116)
14.0	1.79	44 (22)	18 (13)	7.0 (40.0)	−0.137 (0.136)
14.5	1.73	46 (23)	18 (13)	6.0 (40.0)	−0.144 (0.155)
15.0	1.67	47 (23)	18 (13)	5.5 (39.5)	−0.148 (0.163)
15.5	1.62	49 (24)	19 (14)	4.5 (34.0)	−0.138 (0.155)
16.0	1.57	50 (25)	19 (14)	4.0 (29.5)	−0.140 (0.161)
17.0	1.47	50 (26)	20 (15)	3.5 (24.0)	−0.130 (0.156)
18.0	1.39	34 (28)	16 (16)	17.0 (18.5)	0.159 (0.154)
19.0	1.32	36 (29)	17 (17)	14.0 (15.5)	0.155 (0.150)
20.0	1.25	38 (31)	18 (18)	11.0 (12.0)	0.153 (0.148)
21.0	1.19	40 (20)	20 (9)	9.0 (40.0)	0.141 (−0.227)
22.0	1.14	42 (20)	20 (10)	7.5 (40.0)	0.148 (−0.209)
23.0	1.09	43 (21)	21 (10)	6.5 (33.0)	0.146 (−0.216)
24.0	1.04	45 (22)	22 (11)	5.5 (28.0)	0.144 (−0.203)
25.0	1.00	48 (23)	23 (11)	4.5 (23.5)	0.141 (−0.211)

main text, we remind the reader that the results presented in Tables II–V originate from model calculations, which neglect the deformation of the probe due to elastic scattering on the lattice and, as such, they should be valid for very thin specimens. With increasing sample thickness it is expected that the probe phase distribution will distort, which will most likely lead to a reduction of the EMCD signal strength.

The primary optimization condition was for the drift-limited dwell time; see Sec. IV E. Whenever the optimization for dose-limited dwell time led to different results, these are shown in parentheses.

[1] C. Hébert and P. Schattschneider, Ultramicroscopy **96**, 463 (2003).

[2] P. E. Batson, Phys. Rev. Lett. **70**, 1822 (1993).

[3] P. Schattschneider, S. Rubino, C. Hébert, J. Rusz, J. Kuneš, P. Novák, E. Carlino, M. Fabrizioli, G. Panaccione, and G. Rossi, Nature (London) **441**, 486 (2006).

[4] P. Schattschneider, M. Stöger-Pollach, S. Rubino, M. Sperl, Ch. Hurm, J. Zweck, and J. Rusz, Phys. Rev. B **78**, 104413 (2008).

[5] Z. H. Zhang, X. F. Wang, J. B. Xu, S. Muller, C. Ronning, and Q. Li, Nat. Nanotechnol. **4**, 523 (2009).

[6] R. F. Klie, T. Yuan, M. Tanase, G. Yang, and Q. Ramasse, Appl. Phys. Lett. **96**, 082510 (2010).

[7] M. Stöger-Pollach, C. D. Treiber, G. P. Resch, D. A. Keays, and I. Ennen, Micron **42**, 456 (2011).

[8] Z. H. Zhang, H. L. Tao, M. He, and Q. Li, Scr. Mater. **65**, 367 (2011).

[9] J. Salafranca, J. Gazquez, N. Perez, A. Labarta, S. T. Pantelides, S. J. Pennycook, X. Batlle, and M. Varela, Nano Lett. **12**, 2499 (2012).

[10] B. Loukya, X. Zhang, A. Gupta, and R. Datta, J. Magn. Magn. Mater. **324**, 3754 (2012).

[11] Z. Q. Wang, X. Y. Zhong, R. Yu, Z. Y. Cheng, and J. Zhu, Nat. Commun. **4**, 1395 (2013).

[12] S. Muto, J. Rusz, K. Tatsumi, R. Adam, S. Arai, V. Kocevski, P. M. Oppeneer, D. E. Bürgler, and C. M. Schneider, Nat. Commum. **5**, 3138 (2014).

[13] J. Rusz, S. Rubino, and P. Schattschneider, Phys. Rev. B **75**, 214425 (2007)

[14] J. Rusz, O. Eriksson, P. Novák, and P. M. Oppeneer, Phys. Rev. B **76**, 060408(R) (2007).
[15] L. Calmels, F. Houdellier, B. Warot-Fonrose, C. Gatel, M. J. Hÿtch, V. Serin, E. Snoeck, and P. Schattschneider, Phys. Rev. B **76**, 060409(R) (2007).
[16] J. Rusz, S. Rubino, O. Eriksson, P. M. Oppeneer, and K. Leifer, Phys. Rev. B **84**, 064444 (2011).
[17] J. Rusz, S. Muto, and K. Tatsumi, Ultramicroscopy **125**, 81 (2013).
[18] M. Uchida and A. Tonomura, Nature (London) **464**, 737 (2010).
[19] B. J. McMorran, A. Agrawal, I. M. Anderson, A. A. Herzing, H. J. Lezec, J. J. McClelland, and J. Unguris, Science **331**, 192 (2011).
[20] J. Verbeeck, H. Tian, and P. Schattschneider, Nature (London) **467**, 301 (2010).
[21] K. Y. Bliokh, Y. P. Bliokh, S. Savelev, and F. Nori, Phys. Rev. Lett. **99**, 190404 (2007).
[22] G. Van Tendeloo, S. Bals, S. Van Aert, and J. Verbeeck, and D. Van Dyck, Adv. Mater. **24**, 5655 (2012).
[23] J. Rusz and S. Bhowmick, Phys. Rev. Lett. **111**, 105504 (2013).
[24] P. Schattschneider, S. Löffler, M. Stöger-Pollach, and J. Verbeeck, Ultramicroscopy **136**, 81 (2014).
[25] J. Rusz, S. Bhowmick, M. Eriksson, and N. Karlsson, Phys. Rev. B **89**, 134428 (2014).
[26] A. M. Blackburn and J. C. Loudon, Ultramicroscopy **136**, 127 (2014).
[27] A. Béché, R. Van Boxem, G. Van Tendeloo, and J. Verbeeck, Nat. Phys. **10**, 26 (2014).
[28] K. Saitoh, Y. Hasegawa, N. Tanaka, and M. Uchida, J. Electron. Microsc. **61**, 171 (2012).
[29] J. Verbeeck, H. Tian, and A. Béché, Ultramicroscopy **113**, 83 (2012).
[30] O. L. Krivanek, J. Rusz, J.-C. Idrobo, T. J. Lovejoy, and N. Dellby, Microsc. Microanal. **20**, 832 (2014).
[31] J. Verbeeck, P. Schattschneider, S. Lazar, M. Stöger-Pollach, S. Löffler, A. Steiger-Thirsfeld, and G. Van Tendeloo, Appl. Phys. Lett. **99**, 203109 (2011).
[32] J. Rusz, J. C. Idrobo, and S. Bhowmick, Phys. Rev. Lett. **113**, 145501 (2014).
[33] P. D. Nellist, in *Scanning Transmission Electron Microscopy: Imaging and Analysis*, edited by S. J. Pennycook and P. D. Nellist (Springer, New York, 2011), Chap. 2.
[34] Strictly speaking, this represents the optimal symmetry condition. The weakest condition for observing EMCD at the transmitted beam requires only that there is no mirror symmetry plane, with respect to which the phase differences are symmetric.
[35] O. L. Krivanek, N. Dellby, and A. R. Lupini, Ultramicroscopy **78**, 1 (1999).
[36] J. S. Pierce, T. R. Harvey, T. S. Yahn, and B. J. McMorran, Microsc. Microanal. **19**, 1188 (2013).
[37] V. Grillo, G. C. Gazzadi, E. Karimi, E. Mafakheri, R. W. Boyd, and S. Frabboni1, Appl. Phys. Lett. **104**, 043109 (2014).
[38] R. Shiloh, Y. Lereah, Y. Lilach, and A. Arie, Ultramicroscopy **144**, 26 (2014).
[39] J. J. Sakurai and J. J. Napolitano, *Modern Quantum Mechanics* (Addison-Wesley, San Francisco, CA, 2011).
[40] H. Kohl and H. Rose, Adv. Electron. Electron Opt. **65**, 173 (1985).
[41] A. Ankudinov and J. J. Rehr, Phys. Rev. B **51**, 1282 (1995).
[42] M. Haider, H. Mueller, and S. Uhlemann, Adv. Imag. Electron Phys. **153**, 43 (2008).
[43] O. L. Krivanek, G. J. Corbin, N. Dellby, B. F. Elston, R. J. Keyse, M. F. Murfitt, C. S. Own, Z. S. Szilagyi, and J. W. Woo, Ultramicroscopy **108**, 179 (2008).